Journal of Colloid and Interface Science 426 (2014) 72–79

Contents lists available at ScienceDirect

Journal of Colloid and Interface Science

www.elsevier.com/locate/jcis

Combining mercury thermoporometry with integrated gas sorption and mercury porosimetry to improve accuracy of pore-size distributions for disordered solids

Buhari Bafarawa [a], Artjom Nepryahin [a], Lu Ji [b], Elizabeth M. Holt [c], Jiawei Wang [d], Sean P. Rigby [a,*]

[a] Department of Chemical and Environmental Engineering, University of Nottingham, University Park, Nottingham NG7 2RD, United Kingdom
[b] Department of Chemical and Environmental Engineering, University of Nottingham, Ningbo, China
[c] Johnson Matthey, P.O. Box 1, Belasis Avenue, Billingham, Cleveland, United Kingdom
[d] School of Chemical Engineering and Analytical Science, University of Manchester, Manchester M13 9PL, United Kingdom

ARTICLE INFO

Article history:
Received 8 January 2014
Accepted 23 March 2014
Available online 4 April 2014

Keywords:
Porosity
Pore size distribution
Catalyst
Gas sorption
Mercury porosimetry
Thermoporometry

ABSTRACT

The typical approach to analysing raw data, from common pore characterization methods such as gas sorption and mercury porosimetry, to obtain pore size distributions for disordered porous solids generally makes several critical assumptions that impact the accuracy of the void space descriptors thereby obtained. These assumptions can lead to errors in pore size of as much as 500%. In this work, we eliminated these assumptions by employing novel experiments involving fully integrated gas sorption, mercury porosimetry and mercury thermoporometry techniques. The entrapment of mercury following porosimetry allowed the isolation (for study) of a particular subset of pores within a much larger interconnected network. Hence, a degree of specificity of findings to particular pores, more commonly associated with use of templated, model porous solids, can also be achieved for disordered materials. Gas sorption experiments were conducted in series, both before *and* after mercury porosimetry, on the same sample, and the mercury entrapped following porosimetry was used as the probe fluid for theromporometry. Hence, even if one technique, on its own, is indirect, requiring unsubstantiated assumptions, the fully integrated combination of techniques described here permits the validation of assumptions used in one technique by another. Using controlled-pore glasses as model materials, mercury porosimetry scanning curves were used to establish the correct correspondence between the appropriate Gibbs–Thomson parameter, and the nature of the meniscus geometry in melting, for thermoporometry measurements on entrapped mercury. Mercury thermoporometry has been used to validate the pore sizes, for a series of sol–gel silica materials, obtained from mercury porosimetry data using the independently-calibrated Kloubek correlations. The pore sizes obtained for sol–gel silicas from porosimetry and thermoporometry have been shown to differ substantially from those obtained via gas sorption and NLDFT analysis. DRIFTS data for the samples studied has suggested that the cause of this discrepancy may arise from significant differences in the surface chemistries between the samples studied here and that used to calibrate the NLDFT potentials.

1. Introduction

Disordered porous solids, such as sol–gel silicas, are used in many applications, including as catalyst supports or chromatographic media. The performance of these materials in these applications depends strongly upon the structural characteristics of the void space. Experimental methods such as gas sorption or mercury porosimetry are generally used to obtain the pore size distributions (PSDs) for these materials. The most recent data analysis methods, to interpret raw gas sorption isotherm data for disordered materials, have been developed from studies using more ordered, model materials, such as MCM-41 and SBA-15 [1,2]. However, it is not clear that the theories and techniques developed for more regular structures, such as these, will give accurate PSDs for disordered materials with more complex and amorphous internal pore geometry, and more extensive void space interconnectivity. Previous work has suggested that conventional data analysis methods for gas sorption, such as the Barrett–Joyner–Halenda (BJH) algorithm and non-local density functional

* Corresponding author.
E-mail address: enzspr@exmail.nottingham.ac.uk (S.P. Rigby).

http://dx.doi.org/10.1016/j.jcis.2014.03.053
0021-9797/

theory (NLDFT) software, neglect effects such as variations in the causes of hysteresis around the boundary sorption curves, advanced condensation, and delayed adsorption [3–5]. These effects can result in errors of as much as 500% in a PSD [4]. It is thus necessary to both assess the level of systematic error introduced by these effects, and others, into the PSDs for disordered solids, and develop methods to remove this error.

Mercury porosimetry is still a frequently used characterisation method because it remains a rare technique that can provide data over the complete length-scale range from ~3 nm to ~100 μm in a single experiment. Mercury porosimetry relies upon the principle that mercury is a non-wetting fluid for most surfaces, and, thence, ever increasing pressures are required to intrude it into ever smaller pores, according to the Washburn [6] equation. The constant of proportionality between imposed pressure and inverse pore size depends upon the contact angle and surface tension of mercury. The macroscopic contact angle can readily be measured using techniques such as the sessile drop experiment. However, there is often doubt as to whether the macroscopic measurement applies to mercury menisci with a small radius of curvature. Previous workers have attempted to calibrate the physical properties term in the Washburn equation using model materials with independently known pore sizes, such as controlled pore glass (CPG) [7,8].

Frequently, only the mercury porosimetry intrusion curve is used, for the purposes of obtaining a pore neck size distribution, and the extrusion curve is neglected. This is because, in general, the physical processes involved in retraction are more complex than those involved in intrusion. The variety of phenomena involved in retraction, such as contact angle hysteresis, snap-off, and entrapment, mean that interpretations of the retraction curve are often ambiguous, and highly model dependent. However, some workers have attempted to use mercury retraction data to determine pore network connectivity [9] or macroscopic heterogeneity in the spatial distribution of pore size [10]. These attempts at interpreting mercury retraction are often based upon results from glass, plastic or metal micromodels [11,12]. Partly as a means to improve the interpretation of retraction curves, Rigby and co-workers [13–15] introduced the integrated nitrogen sorption and mercury porosimetry technique. This method employs a series of alternating gas sorption and mercury porosimetry experiments carried out on the same single sample, with any mercury entrapped following a porosimetry experiment frozen in place before a subsequent gas sorption experiment is performed. The difference between the gas sorption isotherms before and after mercury entrapment can be used to infer information about the distribution of entrapped mercury, and thence, the retraction process.

In order to interpret properly the mercury porosimetry data from integrated experiments it is necessary to employ calibrated versions of the Washburn equation. Kloubek [8] obtained expressions for the variation of the surface tension and contact angle term with pore size, for both intrusion and extrusion, from the experimental data of Liabastre and Orr [7]. Liabastre and Orr [7] measured the pressures required for intrusion into, and extrusion from, controlled pore glasses (CPGs) for which the pore size could be obtained independently using electron microscopy. Rigby and co-workers [16,17] found that the Kloubek correlations could be used, with no amendments, to remove apparent contact angle hysteresis, and obtain superposition of the intrusion and extrusion curves, for some sol–gel silica materials with the same surface fractal dimension as the original CPG materials used by Liabastre and Orr [7]. Silica materials with different degrees of surface roughness required amendments to the Kloubek correlations to achieve a similar superposition [17]. These trends in the effects of surface roughness on hysteresis were also observed in results from mean-field density functional theory (MFDFT) simulations of mercury intrusion and extrusion on models with rough surfaces [17]. These findings suggested that mercury porosimetry hysteresis was a function of surface chemistry and roughness, and supported the use of the Kloubek [8] correlations to analyse porosimetry data for some sol–gel silicas. As will be seen below, analysing porosimetry data with the Kloubek correlations also allows an estimate to be made of the pore sizes that entrap mercury, but the method is indirect. The validity of the Kloubek correlations will be tested directly using mercury porosimetry scanning loops.

In the integrated method, the gas sorption isotherms can only probe the void space remaining externally accessible, and not the entrapped mercury itself. In this work, thermoporometry, using differential scanning calorimetry (DSC) will be used to probe the entrapped mercury directly. Thermoporometry is the determination of pore sizes from the melting or freezing point depression of fluids imbibed within pores. Previous work [18,19] on the freezing and melting of metals in porous solids has focused more on studying the internal structural changes in the metal, and the freezing and thawing mechanisms, rather than determining pore structural information. Further, where the DSC data was used to infer metal ganglia sizes the relevant Gibbs–Thomson parameter was determined from uncalibrated mercury porosimetry data.

In this work, the calibration of the constants of proportionality in the Washburn and Gibbs–Thomson equation will be given more attention, with a view to studying the consistency of the pore structural information obtained from the three methods, gas sorption, mercury porosimetry, and thermoporometry. The difference between the comparison of results for these different techniques presented here, and that made previously by others [20,21], is that exactly the same sample can be used to make a comparison, and, additionally, that comparison can be further narrowed to a particular sub-set of pores within a disordered material, rather than comparing overall PSDs. Hence, the integrated technique can approach the degree of definitive study permitted for templated model materials, via their high levels of order, but for amorphous, disordered materials. This work will also attempt to reduce the number of arbitrary assumptions that have been necessary for indirect characterisation methods in the past, such as the geometry of the meniscus at the phase transition and the applicability of physical parameters calibrated on model materials. Finally, this work will consider a potential explanation for the discrepancies observed between the different experimental techniques.

2. Experimental

The model material used in this work was the CPG PG24080-10CCM, (purchased from Sigma–Aldrich), denoted CPG1 here. The manufacturers report that the pore size is 24 nm. This has been confirmed by electron microscopy. The other samples used in this work were commercially available sol–gel silica spheres G2, S1 and S2. Details of these materials are given in earlier work [13–15,17].

2.1. Mercury porosimetry

The experiments were carried out using a Micromeritics Autopore IV 9500, which is capable of obtaining pressures of 414 MPa. Prior to any experiment, the samples were dried under vacuum to a temperature of 150 °C for 15 h. The purpose of the thermal treatment was to drive off any physisorbed water content on the sample but leave the morphology of the sample unchanged. Blank corrections were made before the experiments using the formula provided by the manufacturer. The sample, consisting of ~10 pellets, was first evacuated to a pressure of 6.7 Pa under a low pressure analysis in order to remove physisorbed water from the interior of the pore sample. The standard equilibration times used in the experiments were 10 and 30 s, with the two different values

used to check the influence of the length of the equilibration time on the position of porosimetry curves. The mercury porosimetry curves were fully equilibrated at each step.

The basic experimental procedure consists of increasing the external pressure to the sample and thus forcing mercury (non-wetting) into increasingly smaller pores in the solid. The material is first placed in a low pressure port to remove adsorbed gases and vapours. The intruded volume is recorded as a function of pressure thereby yielding an intrusion curve. The pressure was increased incrementally up to a given ultimate pressure up to a maximum of 60,000 psi (414 MPa). Scanning curves involve increasing the pressure only up to a chosen ultimate pressure, in a given experiment, that is less than the maximum possible with the apparatus. The process was reversed by decreasing the pressure stepwise, which allows the mercury to extrude from the solid material, and thus generating an extrusion curve. The increase in the mass of the sample discharged following porosimetry matched the entrapment level anticipated from the porosimetry curves. This demonstrates that the entrapment is real, and not just arising from sample damage.

A control experiment was also conducted to determine whether any mercury would be present in pores not containing mercury left by capillary entrapment. Silica pellet samples were dried in the oven to remove physisorbed water, and then weighed to obtain the dry weight. The dry pellets were then suspended over an open reservoir of liquid mercury (ensuring that neither the sample, nor its support touched the liquid mercury) in a sealed container, and left at a constant temperature of 25 °C for a week. After a week the sample was re-weighed. It was found that there was no significant (i.e. beyond the error in the balance <∼1%) change in the pellet weight. It is noted that, due to the high atomic mass of mercury, the error in the sample weight would correspond to <0.02 of a monolayer of mercury. These results suggest that there is no adsorption of mercury in pores containing vapour phase saturated with mercury vapour. A calculation suggests that the vapour phase in a void space with a characteristic dimension of 50 nm would contain just ∼2 mercury atoms even at mercury saturation pressure at 126 °C.

2.2. Differential scanning calorimetry

Mercury porosimetry was used to prepare the samples used in the DSC experiments. The experiment was carried out using a DSC Q10 V9.8 machine equipped with cooling apparatus and with a data processing system which was used to measure the melting curves of mercury in the silicas. The sample containing mercury was frozen in the DSC cell to the required temperature of −85 °C, and then kept at this temperature for 30 min to ensure temperature homogeneity. After the samples were allowed to come to a thermal equilibrium, the melting curves were measured over the temperature range from −50 °C to −38 °C. The DSC measurements were carried out at low scanning rate, 0.1 °C min^{-1}, to avoid thermal and time delays in the DSC curve. Preliminary studies involving varying the scanning rate indicated that this value was the most appropriate. The DSC has the capability to measure heat flow rates with a resolution of ±0.5 μW and an accuracy of ±2 μW.

2.3. DRIFTS

DRIFTS spectra were collected on a Nicolet iS10 FT-IR spectrometer with a Harrick Praying Mantis high temperature reaction chamber. Sample was ground, sieved to ensure a consistent particle size of less than 75 μm, and packed into the sample holder. The sample was first heated to 300 °C, and then cooled back to 30 °C, under a nitrogen gas flow before taking the spectra in order to mimic the sample preparation procedure for gas sorption experiments. For each spectrum, a total of 64 scans were recorded in the range of 4000–500 cm^{-1} with a nominal resolution of 4 cm^{-1} under N_2 flow. A DRIFTS spectrum of KBr powder was also recorded as a background and subtracted from the spectra of samples automatically by using Nicolet OMNIC.

3. Theory

The size of pore at the onset of mercury entrapment can be determined using the following semi-empirical equation to remove contact angle hysteresis:

$$r = \frac{-A + \sqrt{A^2 - 2BP_{Hg}}}{P_{Hg}} \quad (1)$$

where r is the pore radius (nm) and P_{Hg} the applied pressure (MPa), and A and B are constants that depend upon the material and whether the meniscus is advancing or retreating (see Table 1). For a detailed description of Eq. (1), the reader is referred to previous work of Rigby and Edler [16]. Eq. (1) has been independently calibrated using electron microscopy [7,8]. Additionally, since Eq. (1) has been derived empirically, the calculated error in the pore size is estimated to be ∼4–5% [8]. By removing contact angle hysteresis it means any remaining hysteresis is because of structural effects. For many silica and alumina materials it has been shown that the intrusion and extrusion curves overlay after the mercury porosimetry data has been analysed by Eq. (1) [16].

4. Results

4.1. CPG

Fig. 1 shows the mercury intrusion and extrusion curve data for experiments with ultimate pressures of 414 MPa and 48.2 MPa, and equilibration time of 10 s, for samples of CPG1. The equilibration time did not affect the shape of the curves in the range studied. It can be seen that intrusion up to 414 MPa leads to complete pore-filling, since the top of the intrusion curve exhibits a horizontal plateau at high pressure, and the retraction curve retains a similar flat plateau all of the way down to the pressure when the main extrusion step begins. In contrast, the intrusion curve for the experiment up to only 48.2 MPa is a scanning curve, since it stops while the curve is still ascending, and some retraction starts immediately on reversing the direction of the change in pressure. The width of the hysteresis between intrusion and extrusion is narrower for the scanning curve than for the boundary curve.

Fig. 2(a) shows a DSC melting curve for macroscopic blob of bulk mercury. It shows a relatively sharp peak around the known bulk melting temperature for mercury of −38.8 °C. Fig. 2(b) shows DSC melting curve for the entrapped mercury left after the porosimetry experiment with ultimate intrusion pressure of 414 MPa. The data shows a sharp peak at the known bulk melting point of mercury (∼−39 °C), and a broader, asymmetric peak with a mode at −40.9 °C and a slight tail to lower temperatures both attributed

Table 1
Parameters for insertion into Eq. (1). The advancing meniscus values have a pore radius range of applicability of 6–99.75 nm and the retreating values have a range from 4 to 68.5 nm (d = surface fractal dimension).

	Advancing meniscus		Retreating meniscus	
	A	B	A	B
Silica (d = 2.2–2.3)	−302.533	−0.739	−68.366	−235.561
Silica (d = 2.5)	−302.533	−0.739	−96	−235.561

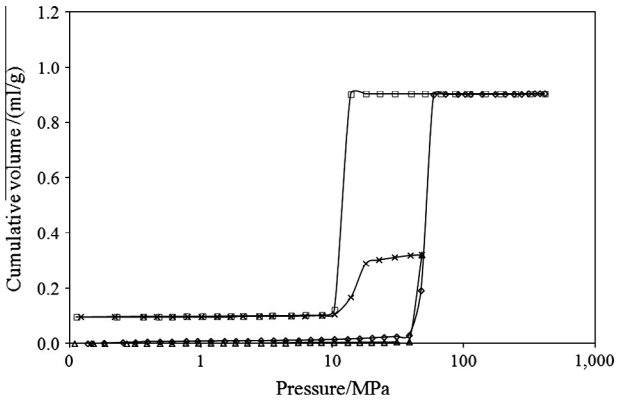

Fig. 1. Mercury intrusion and extrusion curves for porosimetry experiments on samples of CPG1 with ultimate pressures of 414 MPa (◇ intrusion, □ extrusion) and 48.2 MPa (Δ intrusion, × extrusion). The lines shown are to guide the eye.

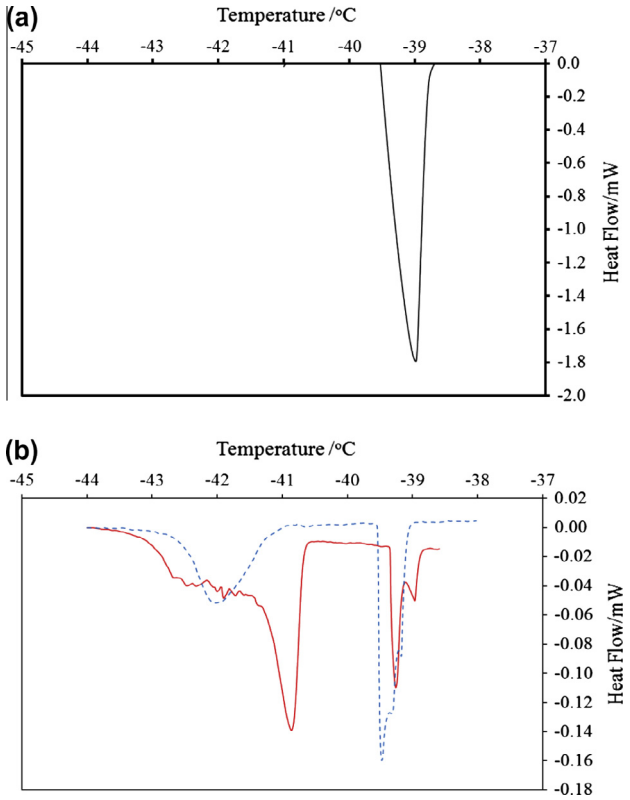

Fig. 2. DSC melting curves for (a) macroscopic droplet of bulk mercury, and (b) entrapped mercury following porosimetry experiments on samples of CPG1 with ultimate pressures of 414 MPa (solid line) and 48.2 MPa (dashed line).

to mercury entrapped within the sample pores. It can thus be seen that the melting point depression of the pore fluid peak relative to the bulk liquid value is 1.9 °C. The atomic diameter of mercury is ~0.3 nm. If the non-freezing, *t*-layer, at the pore walls, is assumed to be 1 atomic diameter thick for mercury ganglia [18,19], then the Gibbs–Thomson parameter from the CPG data is ~45 K nm (based on diameter). If the observed melting is occurring via a cylindrical sleeve meniscus, this implies the Gibbs–Thomson parameter would be 90 K nm for freezing/melting via a hemispherical meniscus. However, if the observed melting of mercury in the CPG is occurring via a hemispherical meniscus, this implies the Gibbs–Thomson parameter would be 22.5 K nm for melting via a cylindrical sleeve meniscus.

Fig. 2(b) also compares the DSC melting curves for entrapped mercury left in a further sample of CPG1 following a mercury intrusion scanning curve up to 48.2 MPa. Both DSC data sets in Fig. 2 show a bulk liquid peak at ~38–39 °C. The presence of shoulders on the main bulk peak may reflect that mercury on the exterior surface of the sample can be confined to cracks and gaps of slightly different sizes/geometries, as well as larger blobs of mercury liquid more like bulk. The variation in the position of the main bulk melting peak suggests the DSC data has an error of ~0.1–0.2 °C. However, it is noted that the mode of the melting peak assigned to the mercury entrapped in the sample following the porosimetry scanning curve occurs at a temperature of ~−42.0 to −42.1 °C, corresponding to a melting point depression of 3–3.1 °C, which is significantly (i.e. greatly exceeds the experimental error) larger than for the sample following intrusion to 414 MPa. This peak for the scanning curve occurs over the same range of temperatures as the broad shoulder on the peak for the full intrusion experiment (up to 414 MPa).

4.2. S1 sol–gel silica

Fig. 3 shows typical mercury intrusion and extrusion curves for a whole pellet sample of S1, and the mercury intrusion and extrusion curves for a fragmented sample of S1, all analysed using the Kloubek [8] correlations. It is noted that the mercury extrusion curve obtained for the fragmented sample overlays the intrusion curve. Using linear interpolation between pore radius points where necessary, the data for the whole pellet and fragmented pellet sample was adjusted to have the same set of pore radius points. The incremental changes in mercury volume over each step in pore radius for the whole pellet extrusion curve were subtracted from those for the powder intrusion/extrusion curve to give the difference plot shown in Fig. 4. The peak in this plot corresponds to pore radii (via the Kloubek [8] correlation) where mercury is apparently getting entrapped. The peak has a baseline range in pore radius from ~5.5 to 9 nm, with the mode at 7.3 nm.

It can be seen from Fig. 3 that, for the whole pellet sample, the mercury extrusion curve follows the mercury intrusion curves for the smallest pores up to a particular pore size, where, thereafter, the extrusion curve deviates from the intrusion curves. Hence, analysis of the mercury porosimetry data for S1 using Eq. (1) leads to an identification of a special point on the mercury intrusion

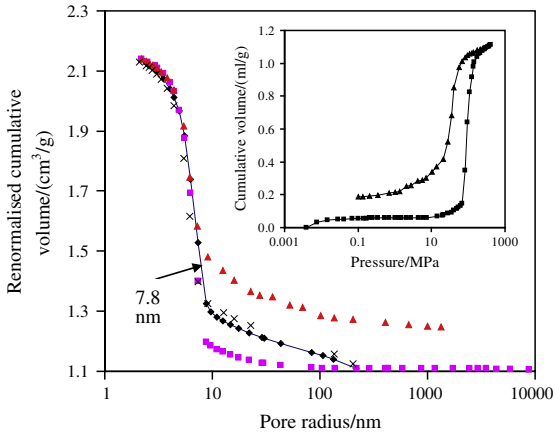

Fig. 3. Mercury porosimetry data for whole (■ intrusion, ▲ extrusion) and powdered (♦ intrusion, × extrusion) samples from batch S1 analysed using semi-empirical alternatives to the Washburn equation [16]. The ultimate intrusion volume for the whole pellet sample has been renormalised to that for the powder sample to facilitate direct comparison of the intra-particle intrusion. The inset shows the raw data for the whole pellet sample. The arrow indicates the position of the modal peak for entrapped mercury from DSC (see below).

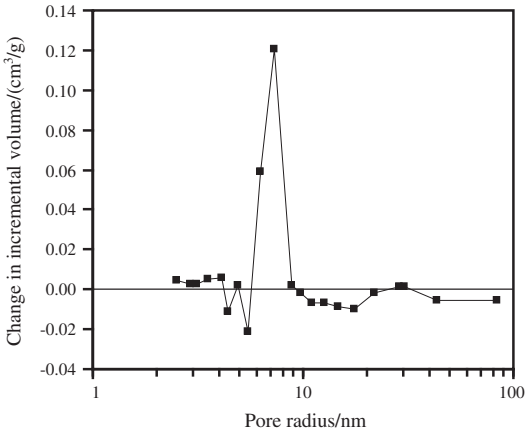

Fig. 4. Variation with pore radius of the difference in incremental volumes (using the same set of pore size bins) between the powder intrusion curve and whole pellet extrusion curve shown in Fig. 3.

curve where the extrusion curve deviates from the intrusion. At the point when the intrusion and extrusion curves diverge, this indicates that less mercury extrudes from the sample compared to the amount that was intruded. This means the pore size where the curves diverge is when mercury entrapment begins. In order to test the validity of the assumptions underlying the application of Eq. (1), a series of porosimetry scanning curves to different ultimate pressures were performed on samples from batch S1, and the level of mercury entrapment at the end of the scanning curves was determined. Fig. 5 shows a plot of the variation in the amount of mercury entrapment following a scanning curve against the pore radius (via the Kloubek correlation) corresponding to the ultimate pressure at the end of the scanning curve. Each data point shown is the mean of a minimum of three samples from the same batch. It can be seen that the entrapment arises predominantly over the particular pore size range ~5–7.3 nm. This range also corresponds to the range covered by the bulk of the asymmetric peak in Fig. 4.

Fig. 6 shows a typical example of a DSC melting curve for a sample of S1 following intrusion in mercury porosimetry up to 414 MPa, and including a reference blob of bulk mercury. The sharp peak at ~−39 °C is the melting of the reference bulk mercury, and is similar to that given in Fig. 2(a). The batch sample mean value of the melting point depression for the lower temperature peak in the melting curve corresponding to the entrapped mercury was 5.8 ± 0.2 °C. The sample mean value for the melting point depression of the tail of this peak was 8 °C. The uncertainty

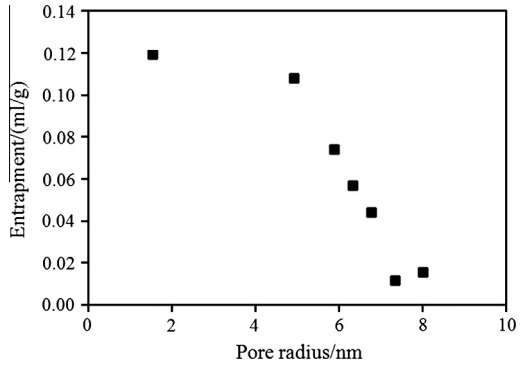

Fig. 5. A plot of the variation in the amount of mercury entrapment following a scanning curve against the pore radius (via the Kloubek [8] correlation) corresponding to the ultimate pressure at the top end of the scanning curve for samples taken from batch S1. Each data point is the sample mean result from at least three samples from batch S1.

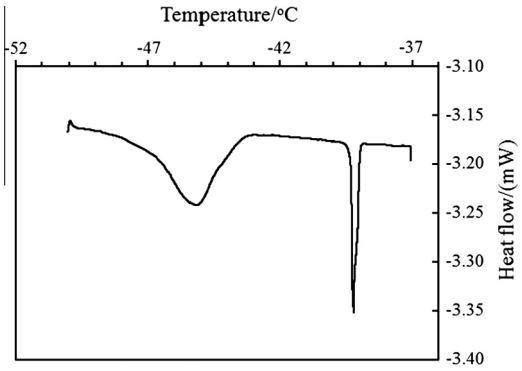

Fig. 6. A typical example of a DSC melting curve for the mercury entrapped within a whole pellet sample of S1 following intrusion in mercury porosimetry up to 414 MPa.

in this value is estimated to be ±1 °C. Using a Gibbs–Thomson parameter of 90 K nm, thereby assuming freezing/melting via a hemispherical meniscus, the pore radii corresponding to the modal peak, and low temperature tail tip, are 7.8 ± 0.3 nm, and 6 ± 1 nm, respectively.

4.3. G2 sol–gel silica

Fig. 7 shows the mercury porosimetry data for a typical whole pellet sample from G2 analysed using Eq. (1) and the parameters for silica given in Table 1. It can be been that Eq. (1) brings the main retraction step into superposition on top of the main intrusion step. The point of deviation between the intrusion and extrusion curves, when entrapment starts, occurs in the pore radius range ~13–16 nm.

Fig. 8 shows the DSC melting curve obtained for the mercury entrapped following the porosimetry experiment that gave rise to the results shown in Fig. 7. The data show a sharp peak from the melting of the bulk mercury droplet, added as a standard, at a temperature similar to that in Fig. 2(a), and a broader peak at lower temperature corresponding to the melting of the entrapped mercury within the pellets. From Fig. 8, it can be seen that the tip of the low temperature tail of the melting peak for the entrapped mercury begins somewhere over the temperature range ~−45 to −43 °C. The tip of the low temperature tail was localised more definitively as follows. The baseline of the data well below the peak region (below −45 °C) was fitted to a straight-line. This straight-line was extrapolated towards the peak region and the residual

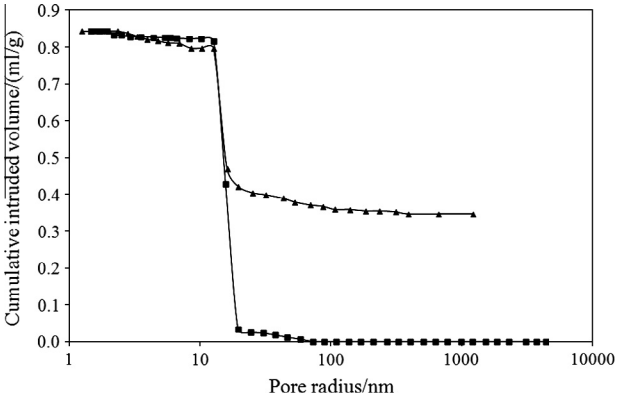

Fig. 7. Mercury porosimetry intrusion (■) and extrusion (▲) data for a typical whole pellet sample from G2 analysed using Eq. (1) and the parameters for silica with surface fractal dimension of 2.3 given in Table 1.

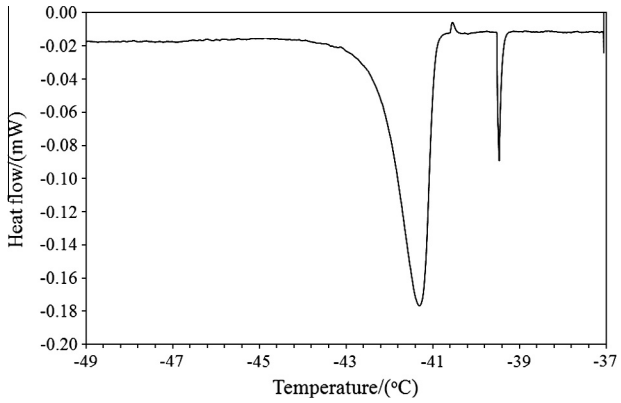

Fig. 8. DSC melting curve obtained for the mercury entrapped following the porosimetry experiment on the sample from batch G2 that gave rise to the results shown in Fig. 7.

between the data-points and the line determined. The residual amplitude was plotted against temperature, and the peak deemed to have commenced when the value of the residual began to systematically climb in value above the general noise level. The peak tail was considered to begin when the residual amplitude typically exceeded three times the standard deviation of the residuals in the region well below the peak. This threshold occurred at −44.3 °C. Using a Gibbs–Thomson parameter of 90 K nm, thereby assuming freezing/melting via a hemispherical meniscus, the pore radii corresponding to the temperature range of the low temperature tail tip was determined as around ∼18 nm. This size is close to that where entrapment begins in the porosimetry data analysed using Eq. (1).

4.4. S2 sol–gel silica

Fig. 9 shows mercury porosimetry data for an experiment on a whole pellet sample from batch S2, with an ultimate intrusion pressure of 414 MPa, that has been analysed using a variant of the Kloubek correlations appropriate to a sample with different

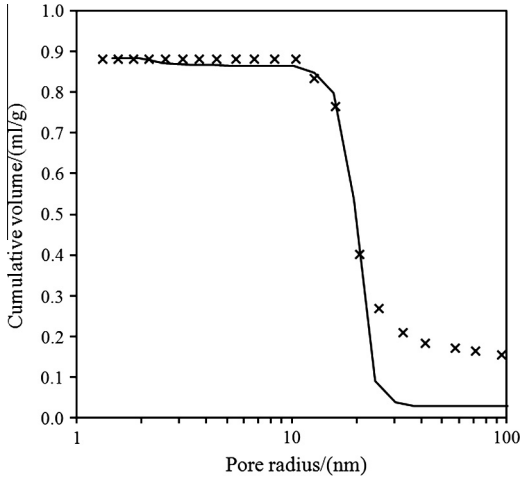

Fig. 9. Mercury porosimetry intrusion (line) and extrusion (×) data. from an experiment on a whole pellet sample from batch S2 with an ultimate intrusion pressure of 414 MPa, that has been analysed using the variant of the Kloubek correlations appropriate to a sample with high surface fractal dimension, given in Table 1.

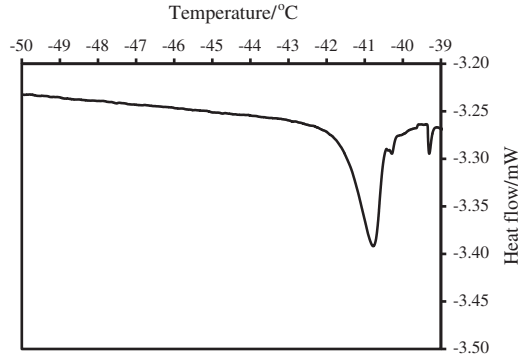

Fig. 10. DSC melting curve data for the entrapped mercury in a sample from batch S2 following mercury intrusion to 414 MPa.

surface roughness to CPG1, S1 and G2. Previous SAXS studies [17] have shown that S2 has a different surface roughness to S1, G2 and the CPGs used to derive the original Kloubek [8] correlation. From Fig. 9 it can be seen that the onset of mercury entrapment occurs over the range of pore sizes ∼20.7–25.4 nm.

Fig. 10 shows the DSC data for a sample from batch S2 following mercury intrusion to 414 MPa. The melting of bulk mercury was observed at −39.3 °C, the modal peak in the melting curve for the mercury in the pores occurs at −40.8 °C, and the low temperature tail of this peak starts at around −43.2 °C. The onset of the low temperature tail of the entrapped mercury melting peak was determined using an analogous method to that used for the corresponding data for G2, with the straight base-line fitted between temperatures of −48 to −44 °C. The melting point depression of the low temperature tail of the melting peak is ∼3.9 °C. Using a Gibbs–Thomson parameter of 90 K nm (based on diameter) the radius of the smallest pores containing entrapped mercury is ∼23–24 nm (using a *t*-layer thickness of 0.3 nm). This is similar to the value of pore size at the onset of mercury entrapment in the mercury porosimetry data.

4.5. DRIFTS

DRIFTS spectra were obtained for the sol–gel silica samples G2, S1, and S2. It was found that the ratios, of the peak corresponding to vicinal/geminal silanols to the peak for single isolated silanols for the same silica, were 10.8, 3.9 and 16.0, for G2, S1 and S2, respectively. These data showed that all three sol–gels had a surface substantially dominated by vicinal/geminal silanols, rather than single isolated silanols.

5. Discussion

The flat plateau at the top of the high pressure mercury intrusion of CPG1 suggests complete pore-filling is achieved. Hence, it is likely that the mercury ganglia would have coalesced throughout the pore network, such that cylindrical-sleeve shaped menisci would have been formed between the mercury thread and the pore walls. In contrast, the immediate decreases in intruded volume on reversal of the direction of pressure change for the scanning curve experiment suggests that free mercury menisci existed at this point. Hence, it seems likely that these free menisci would have been similar to hemispherical in form, since experiments in cylindrical pore models bored through glass suggest intrusion–retraction is piston-like [22]. Therefore it seems likely that the high ultimate pressure intrusion would have created cylindrical sleeve menisci, and the scanning curve would have generated more hemispherical menisci.

The lower melting temperature in the DSC data for the mercury entrapped following the scanning curve porosimetry experiment (up to an ultimate intrusion pressure of 48.2 MPa) on CPG1, is such that the melting point depression is about twice that of the modal melting peak for the mercury entrapped following the full intrusion experiment. Since the scanning curve is likely to give rise to more hemispherical menisci than the full intrusion it seems likely that the melting peak position for the scanning curve experiment corresponds to that for a hemispherical meniscus, and the melting curve peak position for the full intrusion experiment corresponds to that for a cylindrical sleeve meniscus. Hence, overall, the CPG1 DSC data suggest that the Gibbs–Thomson parameter is ~45 K nm (for diameter) melting is occurring via a cylindrical sleeve meniscus, and 90 K nm for freezing/melting via a hemispherical meniscus.

It has been found that, once the appropriate values of the Gibbs–Thomson parameter have been determined for melting according to hemispherical and cylindrical-sleeve menisci in CPG1, those same values can be used to show that the sizes of the pores containing entrapped mercury, in three different sol–gel silicas, obtained using thermoporometry agrees well with the equivalent sizes determined from corresponding mercury porosimetry data and Eq. (1). Hence, these data suggest that thermoporometry can validate pore sizes obtained from mercury porosimetry and Eq. (1).

When the raw mercury porosimetry data is analysed using the Kloubek [8] correlations, and superposition of intrusion and retraction curves is obtained over part of the pore size range, it leads to the identification of a previously undistinguished point on the intrusion curve where deviation from the extrusion curve occurs. This point could be just an artefact of the analysis process but it leads to a prediction about which ultimate pressures of intrusion will lead to any entrapment, or the end of entrapment. This prediction has been tested using scanning curve experiments. It has been found that mercury entrapment in pellets from batch S1 happens for scanning curves with ultimate pressures around that of the point of deviation, and entrapment is virtually non-existent for scanning curve ultimate pressures corresponding to pore sizes above the point of deviation for S1 where intrusion and extrusion curves overlap. Hence, the scanning curve experiments confirm that the point of deviation has physical significance, and is not just an artefact of the data analysis. Therefore, these data validate the use of Eq. (1) to analyse mercury porosimetry data.

The pore sizes obtained from mercury porosimetry and mercury thermoporometry can be compared with those obtained from gas sorption using data from the integrated gas sorption technique. The similarity of gas sorption isotherms obtained for the same sample at a series of different times following porosimetry suggested that entrapped mercury does not migrate over the timescale of the study. Previous work has shown that adsorption in the pores of S1, within which mercury became entrapped, occurred predominantly at a relative pressure of ~0.939 [15]. The cylindrical pore size within which it is expected, from NLDFT, for spinodal condensation to occur at this pressure is 23 nm [2]. The corresponding pore size expected, from NLDFT, to give rise to equilibrium condensation at this same pressure is 42 nm [2]. This compares with a modal pore size (diameter) of 14.6 nm for the pores where entrapment occurs, obtained above from mercury porosimetry and thermoporometry. Hence, the pore size predicted from NLDFT is ~58% higher than obtained via the mercury methods. However, the potentials used in the NLDFT software are calibrated against nitrogen adsorption on aerosil fumed silica [23], and this type of silica has been shown to have a surface dominated by single isolated silanol groups [24]. Hence, since the surface chemistry of the silicas studied here is dominated by vicinal/geminal hydroxyl groups, it is somewhat different to that used to calibrate the NLDFT interaction parameters. Given that the quadrupole of nitrogen is known to interact strongly with the dipole of hydroxyl groups [1], and this affects nitrogen adsorption [25], it seems likely that surface chemistry differences may explain the discrepancy between the two pore size determinations. It is unlikely that surface roughness differences account for the discrepancy between NLDFT and mercury methods, since previous SAXS studies [17] have shown that the surface roughness of aerosil, the CPGs used to obtain the Kloubek correlation, and the sol–gel silicas S1 and G2 were all very similar. Previous work [26] comparing the surface fractal dimensions for S1 and G2 obtained from nitrogen adsorption, with the same parameter obtained from either butane adsorption or SAXS, showed a discrepancy between nitrogen adsorption and the other two techniques. This suggested that the adsorption of nitrogen in these silicas was affected by surface chemical heterogeneity.

6. Conclusions

It has been shown that mercury porosimetry scanning curves can be used to establish the correct correspondence between the appropriate Gibbs–Thomson parameter, and the nature of the meniscus geometry in melting, for thermoporometry measurements using entrapped mercury as the probe fluid. Mercury thermoporometry has been used to validate the pore sizes obtained from mercury porosimetry data using the Kloubek correlations. The pore size obtained for a given sample from porosimetry and thermoporometry has been shown to differ substantially from that obtained via gas sorption and NLDFT analysis. DRIFTS data for the samples studied has suggested that the cause of this discrepancy may arise from significant differences in the surface chemistries between the samples studied here and that used to calibrate the NLDFT potentials.

Therefore, thermoporometry, using mercury entrapped following mercury porosimetry as the probe fluid, has been shown to provide independent validation of pore structural information obtained from porosimetry. Hence, this new type of combined thermoporometry enables independent adjudication of the discrepancy between pore sizes derived from porosimetry and other techniques, such as gas sorption. Our novel use of thermoporometry is thus proposed as a straightforward and essential supplement to porosimetry experiments to ensure greater accuracy of pore size distributions and improved structural characterisation.

Acknowledgments

SPR and AN thank the EPSRC and Johnson Matthey plc for financial support.

References

[1] F. Rouquerol, J. Rouquerol, K. Sing, Adsorption by Powders and Porous Solids: Principles, Methodology and Applications, Academic Press, London, 1999.
[2] A.V. Neimark, P.I. Ravikovitch, Micropor. Mesopor. Mater. 44 (2001) 697–707.
[3] J.M. Esparza, M.L. Ojeda, A. Campero, A. Dominguez, I. Kornhauser, F. Rojas, A.M. Vidales, R.H. López, G. Zgrablich, Colloids Surf., A 241 (2004) 35.
[4] I. Hitchcock, J.A. Chudek, E.M. Holt, J.P. Lowe, S.P. Rigby, Langmuir 26 (2010) 18061–18070.
[5] E. Shiko, J.P. Lowe, K.J. Edler, S.P. Rigby, J. Colloid Interface Sci. 385 (2012) 183–192.
[6] E.W. Washburn, Phys. Rev. 17 (1921) 273–283.
[7] A.A. Liabastre, C. Orr, J. Colloid Interface Sci. 64 (1978) 1–18.
[8] J. Kloubek, Powder Technol. 29 (1981) 63–73.
[9] R.L. Portsmouth, L.F. Gladden, Chem. Eng. Sci. 46 (1991) 3023–3036.
[10] S.P. Rigby, J. Colloid Interface Sci. 224 (2000) 382–396.
[11] N.C. Wardlaw, M. McKellar, Powder Technol. 29 (1981) 127.
[12] R. Leonormand, C. Zarcone, A. Sarr, J. Fluid Mech. 135 (1983) 337–353.
[13] S.P. Rigby, R.S. Fletcher, S.N. Riley, Chem. Eng. Sci. 59 (2004) 41–51.
[14] S.P. Rigby, R.S. Fletcher, Part. Part. Syst. Charact. 21 (2004) 138–148.
[15] S.P. Rigby, P.I. Chigada, E.L. Perkins, M.J. Watt-Smith, J.P. Lowe, K.J. Edler, Adsorption 14 (2008) 289–307.

[16] S.P. Rigby, K.J. Edler, J. Colloid Interface Sci. 250 (2002) 175–190.
[17] S.P. Rigby, P.I. Chigada, Langmuir 26 (2010) 241–248.
[18] Y.A. Kumzerov, A.A. Nabereznov, S.B. Vakhrushev, Phys. Rev. B 52 (1995) 4772–4774.
[19] B.F. Borisov, E.V. Charnaya, P.G. Plotnikov, W.D. Hoffmann, D. Michel, Y.A. Kumzerov, C. Tien, C.S. Wur, Phys. Rev. B 58 (1998) 5329–5335.
[20] I. Beurroies, R. Denoyel, P. Llewellyn, J. Rouquerol, Thermochim. Acta 421 (2004) 11–18.
[21] P.A.C. Gane, C.J. Ridgway, E. Lehtinen, R. Valiullin, I. Furo, J. Schoelkopf, H. Paulapuro, J. Daicic, Ind. Eng. Chem. Res. 43 (2004) 7920–7927.
[22] I. Hitchcock, M. Lunel, S. Bakalis, R.S. Fletcher, E.M. Holt, S.P. Rigby, J. Colloid Interface Sci. 417 (2014) 88–99.
[23] P.I. Ravikovitch, G.L. Haller, A.V. Neimark, Adv. Colloid Interface Sci. 76–77 (1998) 203–226.
[24] B.A. Morrow, A.J. McFarlan, J. Phys. Chem. 96 (1992) 1395–1400.
[25] B.G. Aristov, A.V. Kiselev, Colloid J. USSR 27 (1965) 246–251.
[26] M.J. Watt-Smith, K.J. Edler, S.P. Rigby, Langmuir 21 (2005) 2281–2292.